Earth and Planetary Science Letters 458 (2017) 14–21

Contents lists available at ScienceDirect

Earth and Planetary Science Letters

www.elsevier.com/locate/epsl

Effects of axially variable diking rates on faulting at slow spreading mid-ocean ridges

Xiaochuan Tian [a,b,1], Eunseo Choi [a,*]

[a] Center for Earthquake Research and Information, the University of Memphis, 3890 Central Ave., Memphis, TN, 38152, USA
[b] School of Earth Science and Geological Engineering, Sun Yat-sen University, Guangzhou 510275, PR China

ARTICLE INFO

Article history:
Received 27 June 2016
Received in revised form 12 October 2016
Accepted 16 October 2016
Available online 7 November 2016
Editor: A. Yin

Keywords:
faulting
mid-ocean ridge
diking
detachment
oceanic core complex

ABSTRACT

Magma supply for dike injection can be highly variable within a segment of a slow-spreading mid-ocean ridge but the tectonic impact of this variability is not fully understood. Here, we use three-dimensional numerical models to quantify the effects of variable diking rates on the faulting mode at a 20 km-long slow spreading ridge segment. In addition to end-member faulting modes in which long-lived detachment faults or short-lived normal faults form along the whole segment, we newly identify a transitional mode in which a detachment and a short-lived normal fault form simultaneously but in respective domains separated by a transfer fault. Different faulting modes can be better correlated with the average dike intrusion rate, rather than the highest or lowest rate along the segment. Along-axis stress coupling tends to homogenize fault offset along the segment, inhibiting the domination of a particular faulting mode associated with an extreme local diking rate. This homogenizing effect explains why detachment faults can sometimes form even in the regions previously considered as unfavorable. Our results further suggest that a long (>15 km) and continuous detachment, partially overlain by younger faults, can create an oceanic core complex when faults weaken fast and diking rate is low. When faults weaken slow and diking rate is moderate, however, faulting occurs in the transitional mode, producing a detachment over only a part of the segment length.

© 2016 Elsevier B.V. All rights reserved.

1. Introduction

Modes of faulting at mid-ocean ridges (MORs) are sensitive to the fraction of plate separation that is accommodated by dike intrusion, which is denoted as M (Buck et al., 2005; Tucholke et al., 2008). Numerical models adopting the M-factor parameterization have been successful in explaining major bathymetric contrasts between fast- and slow-spreading ridges (Buck et al., 2005), and variations in faulting and axial morphology in slow to intermediate spreading ridges (Behn and Ito, 2008; Ito and Behn, 2008). M is also useful for quantifying the favorable conditions for the formation of oceanic core complexes (OCCs), where lower crustal or mantle rocks with a corrugated surface are exhumed by a long-lived (>1 Myr) detachment (Cann et al., 1997; Tucholke et al., 1998). Previous modeling studies suggest that OCCs form when M is between 0.3 to 0.5 (Tucholke et al., 2008). When M > 0.5, frequent diking pushes faults away from the ridge axis and, new axial valley faults replace them. This process occurs alternatingly on both sides of the ridge (Buck et al., 2005; Shaw and Lin, 1993), forming symmetric abyssal hills across the ridge axis.

However, recent observations on slow-spreading ridges pose challenges to these models. M values estimated for OCC-forming segments at 13°18′N and 13°48′30″N Mid-Atlantic Ridge (MAR) (MacLeod et al., 2009) can be locally as high as 0.7 (Fig. 1) while as low as 0 to 0.3 at the Atlantis Massif (Grimes et al., 2008) and the Atlantis Bank (Baines et al., 2008). Previous two-dimensional (2D) models cannot fully explain how OCCs can form at location of such high or low M values. In addition, how OCC-forming detachments transition to the abyssal hills-forming normal faults is not clear (MacLeod et al., 2011; Reston and Ranero, 2011). A long-known example is the dome-to-abyssal hills transition found in the Atlantis Massif (Blackman et al., 2008) and a new one is the series of OCCs separated by symmetric abyssal hills between 13°10′N and 13°55′N MAR (MacLeod et al., 2009) (Fig. 1). Clearly, 2D models implicitly assuming that M is uniform along a ridge segment cannot explain these observations.

Addressing these questions requires considering spatially variable M. Especially at slow spreading ridges like the Mid-Atlantic

* Corresponding author.
E-mail address: echoi2@memphis.edu (E. Choi).
[1] Present address: Lamont-Doherty Earth Observatory of Columbia University, Palisades, NY, 10964, USA.

http://dx.doi.org/10.1016/j.epsl.2016.10.033
0012-821X/© 2016 Elsevier B.V. All rights reserved.

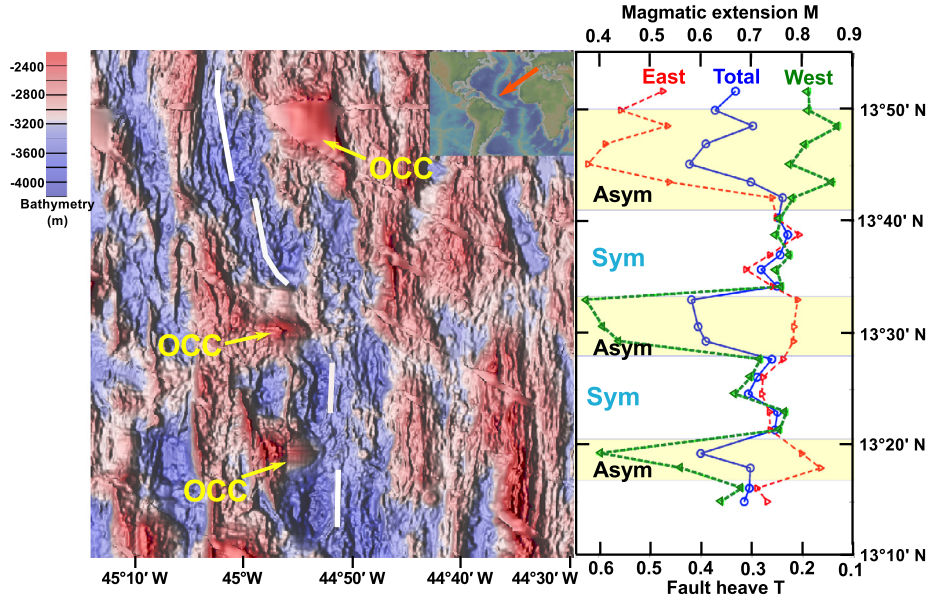

Fig. 1. Bathymetry and the along-ridge variations in M of the Mid-Atlantic Ridge from 13°10′N to 13°55′N. (left) Bathymetry (Ryan et al., 2009) and the inferred axis of the neovolcanic zone (MacLeod et al., 2009) (white lines) with oceanic core complexes (OCCs) annotated. (right) M variations along the ridge adapted from MacLeod et al. (2009). Red and green lines show M variations on the east and the west side of the ridge axis. The mean of the two is the total M (blue line). Fault heave $T = 1 - M$. The yellow shaded areas annotated as "Asym" represent the ridge-parallel extent of asymmetrically spreading OCCs, where the average M is 0.63. The areas annotated as "Sym" show symmetrically spreading abyssal hills and the average M is 0.73.

Ridge (MAR), magma supply is usually higher at the center of the ridge segment and decreases towards the tip of the segment (Carbotte et al., 2015; Lin et al., 1990; Tolstoy et al., 1993). Discrete foci of magmatic accretion along a ridge axis can have wavelengths of 10 to 20 km (Lin et al., 1990). In this study, we investigate how the along-axis variation in magma supply governs the transitions in faulting mode by prescribing variations in M to fully three-dimensional (3D) numerical models.

2. Numerical methods

We use the open source geodynamic modeling code, SNAC (StGermaiN Analysis of Continua) (Choi et al., 2008). SNAC is an explicit Lagrangian finite element code that solves the force and energy balance equations. For each time step, strain and strain rates are updated based on the initial or previous velocity fields under constraints from boundary conditions. A constitutive model returns updated stresses corresponding to these deformation measures. Internal forces are then calculated from the updated stresses and are divided by an artificial mass, which helps damp elastic oscillations, and the resulting accelerations are integrated over time to yield velocities and displacements. A 3D domain is discretized into hexahedral elements, each of which is in turn divided into two sets of tetrahedra. This symmetric discretization prevents faulting from favoring a specific "grain" of a mesh.

Rheology for the oceanic lithosphere is assumed to be elasto-visco-plastic. We use the combination of linear isotropic elasticity, power-law viscosity of dry diabase (Buck et al., 2005; Kirby, 1983) and the Mohr–Coulomb plastic model. We choose rheological structure and parameters that are similar to those used in previous studies (Tucholke et al., 2008) but make further simplifying assumptions such as a steady-state temperature distribution and the use of a single material type for mantle. Weakening of a fault occurs as plasticity goes through strain softening, which is realized by cohesion reduction with an increasing amount of the second invariant of deviatoric plastic strain. We assume this relationship to be linear for simplicity. The initial and final values of cohesion are 44 and 4 MPa. A critical fault offset (Lavier et al., 2000) (ΔX_c), at which cohesion is reduced to a minimum, is used to define the rate of strain weakening. The fault weakening rates based on ΔX_c of 300 m and 1000 m, respectively, are termed "fast" and "slow" in this study. Following previous studies (Buck et al., 2005; Poliakov and Buck, 1998), we also implement a healing process that counteracts the fault weakening process, restoring cohesion in non-deforming regions. In this study, we define the change of plastic strain by healing per time step as $1.0/(1.0 + \Delta t/\tau_h)$, where Δt is the time step and τ_h is the healing time scale, 10^{12} s or ~32 kyrs (Poliakov and Buck, 1998). The complete list of model parameters is given in Table 1.

We follow previous studies to represent the fraction of diking-accommodated plate separation with the 'M' factor (Buck et al., 2005; Poliakov and Buck, 1998). Diking is assumed to occur in the middle of the domain where the lithosphere is the thinnest and dike elements are set to have zero plastic strain. We also calculate pseudo-2D models in order to benchmark against previous studies and to compare with the 3D models. The pseudo-2D model has only one element in the ridge-axis direction to save computational cost and has constant M. All the other settings are the same with 3D models. We verified that pseudo-2D models created with SNAC reproduce the results from selected previous studies (Buck et al., 2005; Tucholke et al., 2008).

The 3D models have a common geometry of $60 \times 20 \times 20$ km (Fig. 2A). The domain is decomposed into 1-km hexahedral elements. Assuming a steady-state temperature field, we reset the temperature field at every time step to a linear profile from 0 °C at a depth of 0 km to 240 °C at 6 km, reflecting enhanced cooling due to hydrothermal circulation, and below 6 km, to the instantaneous cooling of a semi-infinite half-space with plates moving at a constant half-spreading rate of 2.5 cm/yr (Turcotte and Schubert, 2002). Temperature is fixed at 0 °C at the top surface and 1300 °C at the bottom surface. The half spreading rate of 2.5 cm/yr is applied on the model sides that are parallel to the ridge while free-slip boundary conditions are applied to two sides that are perpendicular to the ridge. Hydrostatic seawater pressure is applied on the top surface. Seawater density is assumed to be 1040 kg/m^3. The heights of the water columns are locally determined as $4000 - h(x, z)$ m, where $h(x, z)$ is the topography at horizontal coordinates, x and z. The bottom boundary is free of shear stresses

Table 1
Model parameters.

Input variable	Description	Value	Unit
W_dike	Dike width	2	km
D_dike	Maximum dike depth	8	km
H_axis	Crustal thickness at the axis	6	km
dT/dy	Crustal thermal gradient	40	K/km
T_1	Temperature at lower boundary of crust	240	°C
g	Gravity acceleration	10	m/s^2
demf	Dimensionless force damping factor	0.8	
dt	Time step	0.5	yr
topokappa	Parameter for topography smoothing	0	
shadow_depth	Ghost elements for parallel computing	2	
mesh_i	Mesh number in X direction	60	
mesh_j	Mesh number in Y direction	20	
mesh_k	Mesh number in Z direction	20	
L_i	Length in X direction	60	km
L_j	Length in Y direction	20	km
L_k	Length in Z direction	20	km
rho	Density	3000	kg/m^3
lamda	Lamé's first parameter	30	GPa
mu	Shear modulus	30	GPa
refvisc	Reference viscosity	1.25×10^{-18}	Pa^{-n}/s
activationE	Activation Energy	276	kJ/mol
vis_min	viscosity minimum cutoff	1.00×10^{18}	Pa s
vis_max	viscosity maximum cutoff	1.00×10^{27}	Pa s
srexponent	Power of power law in viscosity	3.05	
epsilon_pi_fast	initial plastic strain for piecewise fast weakening	0	
epsilon_pi_slow	initial plastic strain for piecewise slow weakening	0	
epsilon_pe_fast	end plastic strain for piecewise fast weakening	0.1	
epsilon_pe_slow	end plastic strain for piecewise slow weakening	0.33	
C_i	initial Cohesion for piecewise weakening	44	MPa
C_e	end Cohesion for piecewise weakening	4	MPa
phi	Friction angle	30	°
top_temperature	Surface temperature	0	°C
bottom_temperature	Bottom temperature	1300	°C
V_x	Half spreading rate	7.90×10^{-10}	m/s

and is supported by the Winkler foundation (Buck et al., 2005; Watts, 2001) between remeshings. During remeshing, however, the initial bottom boundary replaces a currently deformed one, essentially allowing in- and outflow of materials.

To consider various spatial patterns of along-axis M variation, we conduct a series of simulations with different combinations of 1) three functional forms for M variation (linear, sinusoidal and square root) (Fig. 2B), 2) five ranges of M variation (0.5–0.7, 0.5–0.8, 0.6–0.8, 0.65–0.9 and 0.8–0.9); and 3) two fault weakening rates ("fast" and "slow"). Table 2 lists all the models presented in this study. In addition, in order to verify that 3D model with constant M is equivalent to the corresponding 2D model, we also run a 3D model with constant $M = 0.8$ along the whole ridge segment and it shows the same faulting behavior as the pseudo-2D model with $M = 0.8$.

3. Results

Our models show four modes of faulting: "asymmetric OCC" (Fig. 2C), "symmetric abyssal hill" (Fig. 2D), "asymmetric abyssal hill" and "transitional mode" (Fig. 2E) (see respective videos in supplementary material). We declare that faulting in a model is in the asymmetric OCC mode when a fault remains active during a total extension greater than $6/(1 - M)$ km. With this amount of total extension, the fault offset approaches the axial lithospheric thickness (6 km) (Buck, 1993) and the fault starts exposing lower crustal and upper mantle materials onto the surface. When a new near-axis fault repeatedly replaces an old fault that has not become a detachment yet, the symmetric abyssal hill mode is declared. In the transitional mode, these two faulting modes appear in one model. A detachment that forms near the low-M end of the ridge produces an OCC while abyssal hills bounded by short-lived normal faults form in the higher-M portion of the segment. A transfer fault forms and becomes a boundary between the domains of the OCC and the abyssal hill modes. However, the formation of the transfer fault is not a sufficient condition for the transitional model.

The faulting modes are sensitive to both fault weakening rates and segment average of M ($\overline{M}$) but not to the smallest or the greatest value in the prescribed range of M. Fig. 2C shows a model in the asymmetric OCC mode. It has the "fast" fault weakening rate and an M variation that changes from 0.5 to 0.8 as a square root function of along-axis distance. $\overline{M}$ is 0.69. A high angle normal fault initiates at the low M side of the segment where stresses due to plate stretching build up faster than in the higher M regions. Faulting propagates towards the high M side, making a segment-long fault (Fig. 2C_1). This fault develops greater offset and associated footwall rotation at the low M side than at the high M side, generating shear and torsional motions around an axis parallel to the ridge axis. The fault rotates to a low dip, becoming a whole-segment detachment (Fig. 2C_2). The stresses due to non-uniform offset and the sufficiently low strength of the detachment together promote the formation of an whole-segment OCC even at the high-M end where M is locally as high as 0.8. With further extension, a ~10 km-long portion from the high-M end is eventually replaced by a new near-axis fault (Fig. 2C_3). The rest of the detachment remains active and rooted at the spreading center. Later, the new near-axis fault forms and produces a "rider block" overlying the high-M portion of the original whole-segment detachment fault.

When only the fault weakening rate is switched to "slow" in the above model, faulting occurs in the symmetric abyssal hill mode (Fig. 2D). The evolution of this model is similar to that of the previous up to the formation of a segment-long fault (Fig. 2D_1). Compared to the fast-weakening model in Fig. 2C, however, the slower weakening rate appears to make the high- and the low-M end of the ridge more tightly coupled, permitting relatively small

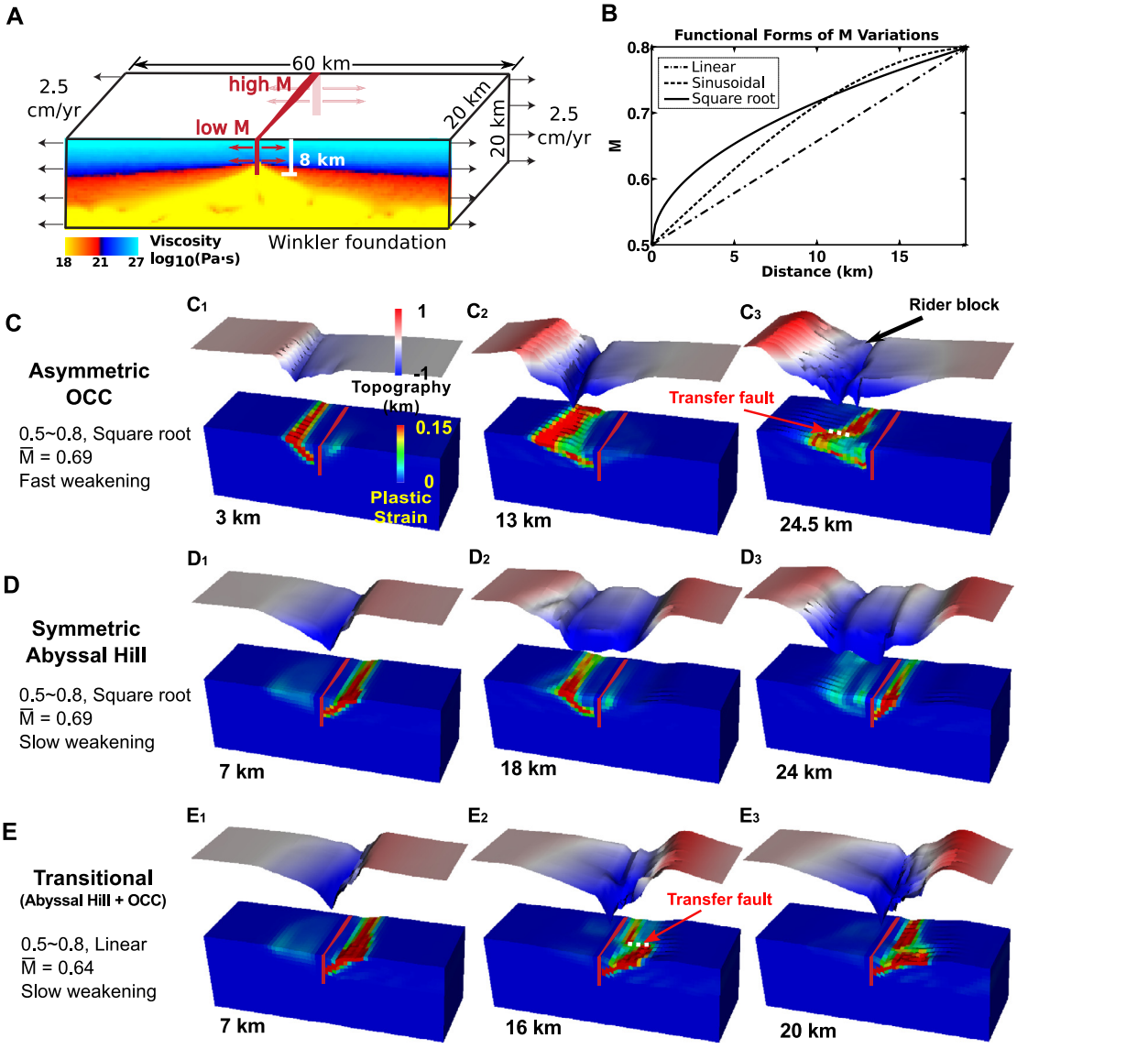

Fig. 2. Model setup and the modes of faulting. **A.** The model geometry and the initial viscosity distribution with boundary conditions annotated. **B.** Three functional forms of M variation along the ridge axis. **C.** Snapshots of the surface topography (vertical exaggeration of 5) and plastic strain representing faults from a model in the asymmetric OCC mode, arranged in the increasing order of total extension. The model has a square-root variation of M between 0.5 and 0.8 and the "fast" fault weakening rate. **D.** Same as C but from a model in the symmetric abyssal hill mode. The "slow" fault weakening is the only difference from the model in C. **E.** Same as C but from a model in the transitional mode. The linearly varying M between 0.5 and 0.8 is the only difference from the model shown in D.

difference in the offset and the amount of footwall rotation along the ridge. Under the tight coupling, the entire segment locks without forming a detachment even at the low-M end, where M approaches 0.5, the most favorable value for OCC formation (Buck et al., 2005; Tucholke et al., 2008). Subsequently, the whole-segment initial fault is replaced by another segment-long fault forming on the other side of the ridge (Fig. 2D_2). Repeatedly occurring, this process produces short-lived normal faults alternating on each side of the ridge axis. The fault alternation produces abyssal hills that are symmetric across the ridge axis (Fig. 2D_3).

The transitional mode of faulting occurs in a model that also has slow weakening but differs from the one in Fig. 2D only in that M varies linearly from 0.5 to 0.8, lowering $\overline{M}$ from 0.69 to 0.64 (Fig. 2E). During the first 15 km of extension, this model also develops a segment-long fault (Fig. 2E_1). However, as visualized in Fig. 2B, M values of the linear model is consistently smaller than those of the square root model. In other words, M is everywhere closer to the range of 0.3–0.5 where OCC's occur in 2D cases. The initial segment-long fault stays active longer than in the square

Table 2
List of 3D models.

Model	M	Functional form	$\overline{M}$	Rate of weakening	Faulting mode
1	0.5–0.7	Linear	0.60	Fast	Oceanic Core Complex (OCC)
2		Square root	0.63	Fast	OCC
3		Linear	0.60	Slow	OCC
4		Sinusoidal	0.62	Slow	OCC
5	0.5–0.8	Sinusoidal	0.68	Fast	OCC
6		Square root	0.69	Fast	OCC
7		Linear	0.64	Slow	Transitional
8		Sinusoidal	0.68	Slow	Symmetric Abyssal Hills (SAH)
9		Square root	0.69	Slow	SAH
10	0.6–0.8	Sinusoidal	0.72	Fast	Asymmetric Abyssal Hills (AAH)
11	0.65–0.9	Sinusoidal	0.8	Fast	AAH
12	0.8–0.8	Constant	0.8	Slow	SAH
13	0.8–0.9	Sinusoidal	0.86	Fast	SAH

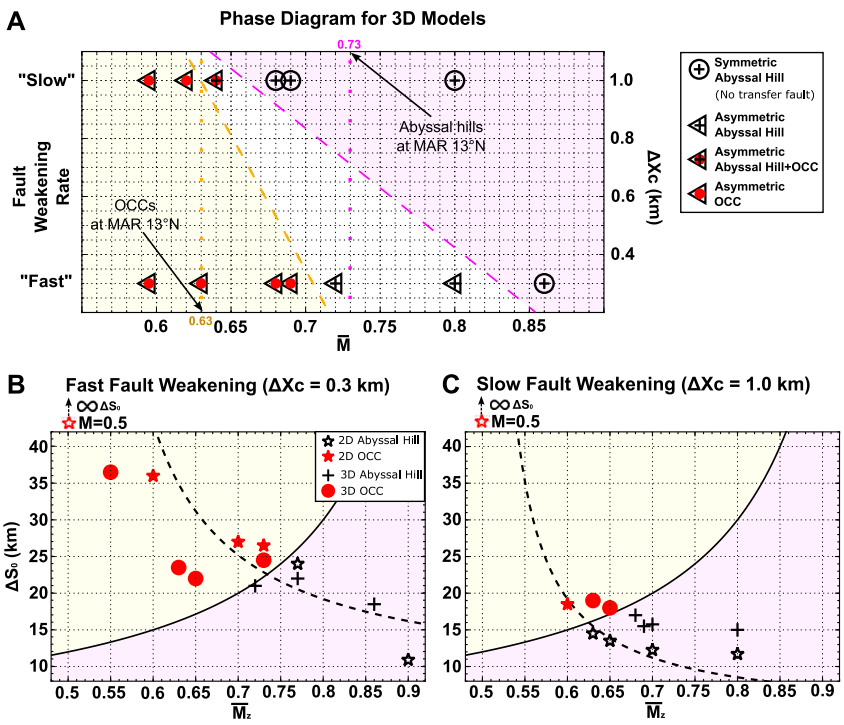

Fig. 3. Sensitivity of faulting modes to fault weakening rates, the whole-segment average of M ($\overline{M}$), the average M of the partially locking portion of the segment ($\overline{M}z$) and the total extension until the locking of the first fault (ΔS_0). **A.** Faulting modes of the 3D models as a function of fault weakening rates and $\overline{M}$. Yellow and pink regions with the inferred boundaries (yellow and pink dashed lines) denote the stability fields of the asymmetric OCC and the symmetric abyssal hill modes, respectively. The estimated $\overline{M}$ values for OCCs (0.63) and abyssal hills (0.73) at MAR 13°N (Fig. 1) (MacLeod et al., 2009) are shown as well. Transfer faults form in all the faulting modes except the symmetric abyssal hill mode. **B.** Faulting modes of the fast-weakening (i.e., $\Delta X_c = 0.3$ km) 2D and 3D models plotted in terms of ΔS_0 and $\overline{M}z$. The black solid line is the boundary for OCC vs. Abyssal Hill formation: $\Delta S_0 = 6/(1 - \overline{M}z)$. Dashed line is the simplistic prediction of fault spacing as a function of $\overline{M}z$ (Behn and Ito, 2008; Buck et al., 2005): $\Delta S_0 = x_{AF}\ \overline{M}z/(\overline{M}z - 0.5)$, where x_{AF} denotes the distance the active fault is transported off-axis before the formation of the new fault and is set to be 7.2 km to reasonably fit the trend of 2D data. **C.** Same as B but for the slow-weakening 2D and 3D models with $\Delta X_c = 1.0$ km. Dashed line corresponds to $x_{AF} = 3.2$ km. (For interpretation of the references to color in this figure, the reader is referred to the web version of this article.)

root model, sustaining greater shear and torsional motions arising from non-uniform fault offset. It does not evolve into a whole-segment detachment as in Fig. 2C, either, because the formation of a new near-axis fault at high-M side is promoted in the case of the slow weakening. As a result, a transfer fault, orthogonal to the ridge axis, forms (Fig. 2E_2) and decouples the high- and low-M portions. The first fault's 8 km-long portion from the low-M end becomes an OCC-forming detachment while the high-M portion "locks" as the "inward fault jump" process occurs as first described in Tucholke et al. (1998) (Fig. 2E_3). This faulting mode is asymmetric in the sense that all the newly created faults form on the same side with the first fault. Locking of the high-M portion of the first fault occurs in the asymmetric OCC mode as well (Fig. 2C_3) but the key difference is that the transitional mode does not produce a segment-long detachment fault.

4. Discussion and conclusions

We summarize the impact of fault weakening rates and M variations on the modes of faulting in Fig. 3A. When the fault weakening is "slow", the asymmetric OCC and symmetric abyssal hill modes will appear when $\overline{M} \leq 0.63$ and ≥ 0.66, respectively. The transitional mode appears in the in-between values of $\overline{M}$ although the $\overline{M}$ range in which this mode is stable cannot be accurately determined with the discrete set of models. The "fast" weakening rate enlarges the stability field of the OCC mode ($\overline{M} \leq 0.705$) and shrinks the $\overline{M}$ range for the symmetric abyssal hill mode ($\overline{M} \geq 0.83$). This trend is consistent with the general tendency that fast fault weakening promotes the formation of detachment faults (Lavier et al., 2000). In contrast to the slow-weakening cases, the transitional mode is not observed among the fast-weakening models but the abyssal hill formation becomes one-sided or asymmetric when $\overline{M}$ is greater than 0.705 and less than 0.83.

Transfer faults form in all the models that are not in the symmetric abyssal hill mode (e.g., Fig. 2C and E), indicating that they form whenever there is sufficient difference in fault offset and footwall rotation along the ridge axis. The slow-weakening models develop transfer faults that are clearly recognizable and orthogonal to the ridge axis when the initial fault is segmented. However, the fast-weakening models do not always develop as well-defined transfer faults as the slow-weakening ones do. Also, the location of transfer faults and the timing of their formation are highly variable among the fast-weakening models. Proper investigation on the systematics of transfer faults would require higher-resolution models.

$\overline{M}$ values of the OCCs and the abyssal hills between 13°10′N and 13°55′N MAR (MacLeod et al., 2009) (Fig. 1) are estimated to be 0.63 and 0.73, respectively. If we assume that the OCC and the abyssal hill faulting modes were active at the same time in this region, we can conclude based on Fig. 3A that faults in this region should weaken relatively slowly (i.e., $0.7 < \Delta X_c < 1$) in the scale of this study.

One of the unique characteristics of the 3D models with variable M is the mechanical interaction between the high- and low-M regions. To highlight the consequences of the interaction, we compare our 3D models with 2D models free of M variation. To reduce complexity involved in the comparison, we focus on ΔS_0, the total extension until the locking of the first fault, which occurs when a new fault replaces the first fault. Since the high- and low-M portions of the first segment-long fault of a 3D model tend to lock at different times, we define ΔS_0 of the 3D model to be that of any portion that locks. Thus, we represent a 3D model with $\overline{M}z$, the

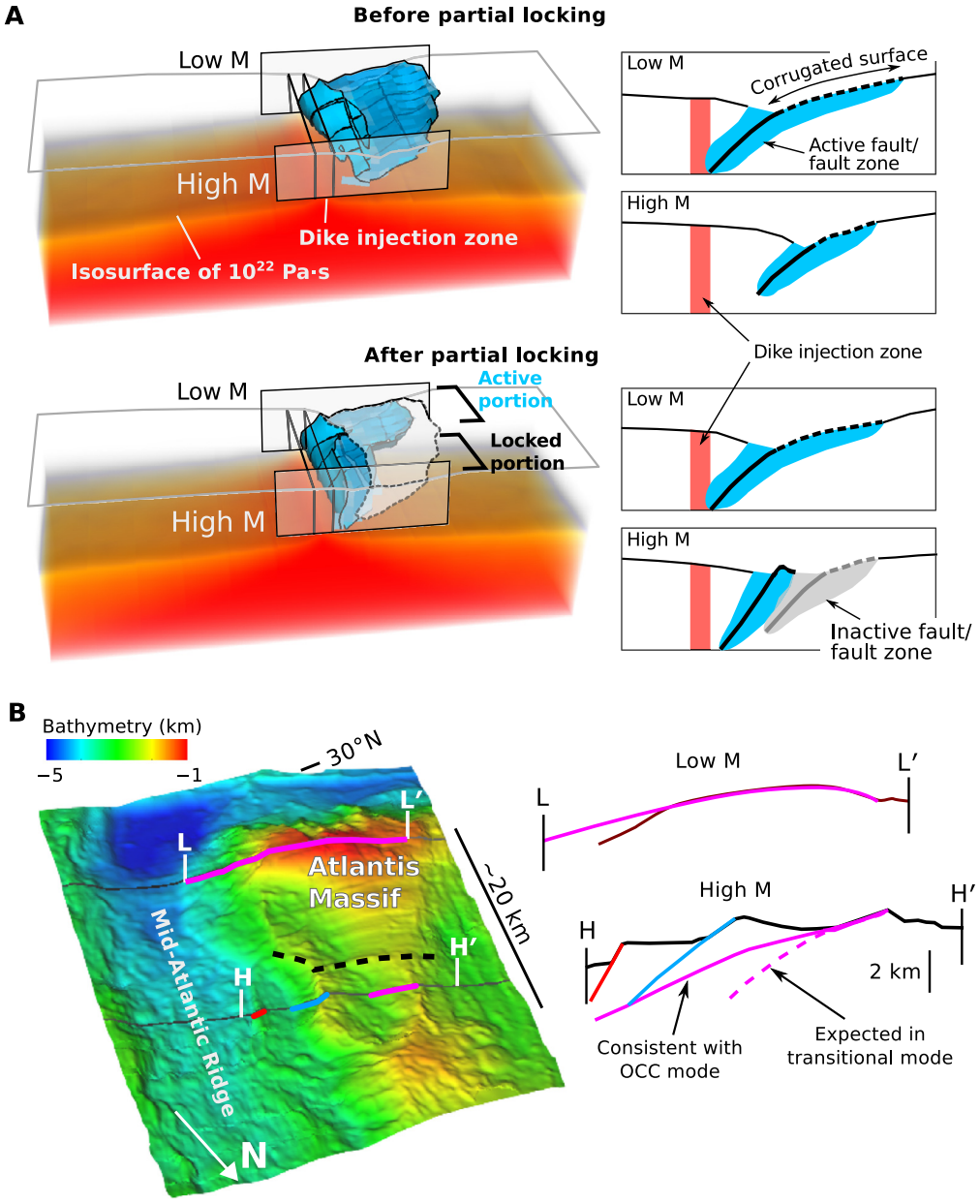

Fig. 4. A. Detailed comparison of fault geometry of the model shown in Fig. 2E before and after the formation of a higher angle normal fault at the high M side. (left) The distribution of viscosity from 10^{18} Pa s (red) to 10^{22} Pa s (yellow) and the blue-colored isosurface for 5% second invariant of deviatoric plastic strain. The outline of the top surface and the locations of the cross-sections are also shown. (right) Drawings of interpreted fault geometry on the cross-sections at the low- and the high-M end. **B**. Bathymetry (left) and cross-sections (right) of the Atlantis Massif. The locations and structural interpretations of the cross-sections are adapted from Reston and Ranero (2011). The black dashed line on the bathymetry plot is an inferred boundary between OCC and abyssal hills. The magenta solid and dashed lines on the cross section H–H′ are fault geometries expected for the asymmetric OCC and the transitional mode, respectively. (For interpretation of the references to color in this figure, the reader is referred to the web version of this article.)

average M only over the very first locking portion of the first fault that forms. A 2D model is said to "correspond" to the locked portion of a 3D model if it has M equal to the 3D model's $\overline{M}z$. In all cases of the "symmetric abyssal hill mode", the initial fault locks along its full length at approximately the same time. Thus in this case $\overline{M}z$ is equal to $\overline{M}$. In contrast, in the case of "OCC" or "Transitional" modes, the higher-M portions of the fault locks well before the lower-M portions, and thus $\overline{M}z > \overline{M}$. M, $\overline{M}$ and $\overline{M}z$ of a 2D model always coincide.

For fast-weakening models, the 3D models show consistently smaller ΔS_0 than the corresponding 2D models (Fig. 3B). A segment-long fault in the 3D models initiates at the low-M end and propagates towards the high-M end. This process makes faulting around the high-M end start earlier in the 3D models than in the corresponding 2D models. The fault initiated early in the high-M region can end up locking earlier than the first fault in the corresponding 2D model, resulting in smaller ΔS_0 values. Locking of the first fault more often occurs in the mid- to low-M regions (see supplementary movies MidMLocking.mov and LowMLocking.mov in the supplementary material) and ΔS_0 values of such 3D models are still smaller than those of the corresponding 2D models. Initiating a fault in the high-M region and keeping it active would require extra work in addition to the energy required for maintaining an active fault in the mid- to low-M regions. As a result, creating a new near-axis fault in the mid- to low-M regions might become energetically favorable after a smaller amount of total extension (i.e., smaller ΔS_0) in the 3D models than in the corresponding 2D models.

In contrast, ΔS_0 values of the slow-weakening 3D models are consistently greater than that of the corresponding 2D models by 2 to 4 km (Fig. 3C). The higher rate in accumulating fault offset and footwall rotation on the low-M portion of the first fault can assist the high-M portion to remain active through mechanical coupling until a mature transfer fault shuts off the mechanical interaction. However, a transfer fault would take a greater amount of offset, which is proportional to the total extension, to fully weaken in models with a slow fault weakening than in those with a fast weakening rate. These effects seem to make the slow-weakening 3D models have greater ΔS_0 than the corresponding 2D models. The mechanical interaction also explains why the OCC-to-abyssal hill transition occurs at higher value of $\overline{M}z$ ($\sim$0.66) in 3D than in 2D ($\sim$0.61). They need higher $\overline{M}z$ to push the hanging wall off axis faster to counterbalance the effects of along ridge coupling that tends to prolong how long the fault can last.

It has been unclear whether and why an oceanic detachment fault can have an along-axis extent much greater than the typical ridge-parallel dimension of the corrugated surfaces of 15–25 km (Smith et al., 2006; Spencer, 1999). One hypothesis (Reston and Ranero, 2011) is that detachments are generally much greater in along-strike extent but might be locally buried under "rider blocks", pieces of the hangingwall cut by newly forming median valley faults. The other possibility (MacLeod et al., 2009) is that the along-axis extent of a detachment is limited to the ridge-parallel dimension of the exposed corrugated surfaces. Our models show both are possible. In the asymmetric OCC mode, the initial segment-long detachment fault can be locally replaced in the role of accommodating plate separation by a new high-angle median-valley fault in the high M regions and overlain by a rider block (Fig. 2C). Although our models do not involve sedimentary or volcanic filling in the median valley of which importance for the rider block formation was emphasized previously (Choi et al., 2013; Reston and Ranero, 2011), this mode provides a possible mechanical process of the formation of a long and continuous detachment fault, which was proposed based on the seismically imaged structure of the Atlantis Massif (Reston and Ranero, 2011). Contrastingly, in the transitional mode, the high-M portion of the segment-long first fault starts producing the abyssal hills, not becoming a part of an OCC-forming detachment (Fig. 4A). Also, the OCC and the abyssal hills are separated by a transfer fault. These characteristics can be viewed as consistent with the detachment exposed at the central dome of the Atlantis Massif and the basaltic abyssal hills to the north (Blackman et al., 2008) (Fig. 4B). Strike-slip focal mechanisms on the north-facing scarp of the Southern Ridge (Collins et al., 2012) suggests the possibility of a transfer fault in the Atlantis Massif. The series of OCCs separated by symmetric abyssal hills between 13°10′N and 13°55′N MAR (MacLeod et al., 2009) (Fig. 1) might also correspond to the transitional mode.

Acknowledgements

Authors thank Texas Advanced Computing Center for providing allocations on Stampede, where many of the numerical models have been run, as well as Dr. Jie Liu and Dr. Ke Zhang from Sun Yat-sen University for generously granting access to Tianhe-2 on which some models were run. Authors also thank Garrett Ito for meticulous and extremely helpful comments and an anonymous reviewer for pointing to interesting and pertinent issues. XT is grateful to W.R. Buck for constructive suggestions on quantifying the along-ridge coupling effects.

Appendix A. Supplementary material

Supplementary material related to this article can be found online at http://dx.doi.org/10.1016/j.epsl.2016.10.033.

The version of SNAC used for this study and the complete set of input files for the models listed in Table 2 are available at https://github.com/kelchuan/snac-1/tree/waterp. Also, the movies of the models that are listed in Table 2 but not included in the Supplementary Material are available at https://dx.doi.org/10.6084/m9.figshare.4083240.v1 and 10.6084/m9.figshare.4083219.v1.

References

Baines, A.G., Cheadle, M.J., John, B.E., Schwartz, J.J., 2008. The rate of oceanic detachment faulting at Atlantis Bank, SW Indian Ridge. Earth Planet. Sci. Lett. 273, 105–114.

Behn, M.D., Ito, G., 2008. Magmatic and tectonic extension at mid-ocean ridges: 1. Controls on fault characteristics. Geochem. Geophys. Geosyst. 9, Q08O10. http://dx.doi.org/10.1029/2008GC001965.

Blackman, D., Karner, G.D., Searle, R.C., 2008. Three-dimensional structure of oceanic core complexes: effects on gravity signature and ridge flank morphology, Mid-Atlantic Ridge, 30°N. Geochem. Geophys. Geosyst. 9, Q06007. http://dx.doi.org/10.1029/2008GC001951.

Buck, W.R., 1993. Effect of lithospheric thickness on the formation of high- and low-angle normal faults. Geology 21, 933. http://dx.doi.org/10.1130/0091-7613(1993)021<0933:EOLTOT>2.3.CO;2.

Buck, W.R., Lavier, L.L., Poliakov, A.N.B., 2005. Modes of faulting at mid-ocean ridges. Nature 434, 719–723. http://dx.doi.org/10.1038/nature03358.

Cann, J.R., Blackman, D.K., Smith, D.K., McAllister, E., Janssen, B., Mello, S., Avgerinos, E., Pascoe, A.R., Escartin, J., 1997. Corrugated slip surfaces formed at ridge-transform intersections on the Mid-Atlantic Ridge. Nature 385, 329–332. http://dx.doi.org/10.1038/385329a0.

Carbotte, S.M., Smith, D.K., Cannat, M., Klein, E.M., 2015. Tectonic and magmatic segmentation of the Global Ocean Ridge System: a synthesis of observations. Geol. Soc. (Lond.) Spec. Publ. 420. http://dx.doi.org/10.1144/SP420.5.

Choi, E., Buck, W.R., Lavier, L.L., Petersen, K.D., 2013. Using core complex geometry to constrain fault strength. Geophys. Res. Lett. 40, 3863–3867. http://dx.doi.org/10.1002/grl.50732.

Choi, E., Lavier, L., Gurnis, M., 2008. Thermomechanics of mid-ocean ridge segmentation. Phys. Earth Planet. Inter. 171, 374–386. http://dx.doi.org/10.1016/j.pepi.2008.08.010.

Collins, J.A., Smith, D.K., McGuire, J.J., 2012. Seismicity of the Atlantis Massif detachment fault, 30N at the Mid-Atlantic Ridge. Geochem. Geophys. Geosyst. 13, 1–14. http://dx.doi.org/10.1029/2012GC004210.

Grimes, C.B., John, B.E., Cheadle, M.J., Wooden, J.L., 2008. Protracted construction of gabbroic crust at a slow spreading ridge: constraints from $^{206}Pb/^{238}U$ zircon ages from Atlantis Massif and IODP Hole U1309D (30°N, MAR). Geochem. Geophys. Geosyst. 9, Q08012. http://dx.doi.org/10.1029/2008GC002063.

Ito, G., Behn, M.D., 2008. Magmatic and tectonic extension at mid-ocean ridges: 2. Origin of axial morphology. Geochem. Geophys. Geosyst. 9, Q09012. http://dx.doi.org/10.1029/2008GC001970.

Kirby, S.H., 1983. Rheology of the lithosphere. Rev. Geophys. 21, 1458. http://dx.doi.org/10.1029/RG021i006p01458.

Lavier, L.L., Buck, W.R., Poliakov, A.N.B., 2000. Factors controlling normal fault offset in an ideal brittle layer. J. Geophys. Res. 105, 23431. http://dx.doi.org/10.1029/2000JB900108.

Lin, J., Purdy, G.M., Schouten, H., Sempere, J.-C., Zervas, C., 1990. Evidence from gravity data for focused magmatic accretion along the Mid-Atlantic Ridge. Nature. http://dx.doi.org/10.1038/344627a0.

MacLeod, C., Searle, R.C., Murton, B.J., Casey, J.F., Mallows, C., Unsworth, S.C., Achenbach, K.L., Harris, M., 2009. Life cycle of oceanic core complexes. Earth Planet. Sci. Lett. 287, 333–344.

MacLeod, C.J., Searle, R.C., Mallows, C., Young, E.C., 2011. Hidden tectonics at slow-spreading ridges: distinguishing magmatic from tectonic spreading. Abstr. T31D-06 Present. 2011 Fall Meet. AGU, San Fr. Calif., 5–9 Dec.

Poliakov, A.N.B., Buck, W.R., 1998. Mechanics of stretching elastic–plastic–viscous layers: applications to slow-spreading mid-ocean ridges. In: Geophysical Monograph Series, pp. 305–323.

Reston, T.J., Ranero, C.R., 2011. The 3-D geometry of detachment faulting at mid-ocean ridges. Geochem. Geophys. Geosyst. 12, Q0AG05. http://dx.doi.org/10.1029/2011GC003666.

Ryan, W.B.F., Carbotte, S.M., Coplan, J.O., O'Hara, S., Melkonian, A., Arko, R., Weissel, R.A., Ferrini, V., Goodwillie, A., Nitsche, F., Bonczkowski, J., Zemsky, R., 2009. Global multi-resolution topography synthesis. Geochem. Geophys. Geosyst. 10, Q03014. http://dx.doi.org/10.1029/2008GC002332.

Shaw, P.R., Lin, J., 1993. Causes and consequences of variations in faulting style at the Mid-Atlantic Ridge. J. Geophys. Res. 98, 21839–21851. http://dx.doi.org/10.1029/93JB01565.

Smith, D.K., Cann, J.R., Escartín, J., 2006. Widespread active detachment faulting and core complex formation near 13° N on the Mid-Atlantic Ridge. Nature 442, 440–443. http://dx.doi.org/10.1038/nature04950.

Spencer, J.E., 1999. Geologic continuous casting below continental and deep-sea detachment faults and at the striated extrusion of Sacsayhuamán,

Peru. Geology 27, 327–330. http://dx.doi.org/10.1130/0091-7613(1999)027<0327:GCCBCA>2.3.CO;2.

Tolstoy, M., Harding, A.J., Orcutt, J.A., 1993. Crustal thickness on the Mid-Atlantic Ridge: bull's-eye gravity anomalies and focused accretion. Science 80 (262), 726–729. http://dx.doi.org/10.1126/science.262.5134.726.

Tucholke, B.E., Behn, M.D., Buck, W.R., Lin, J., 2008. Role of melt supply in oceanic detachment faulting and formation of megamullions. Geology 36, 455–458. http://dx.doi.org/10.1130/G24639A.1.

Tucholke, B.E., Lin, J., Kleinrock, M.C., 1998. Megamullions and mullion structure defining oceanic metamorphic core complexes on the Mid-Atlantic Ridge. J. Geophys. Res. 103, 9857–9866. http://dx.doi.org/10.1029/98JB00167.

Turcotte, D.L., Schubert, G., 2002. Geodynamics. Cambridge University Press, Cambridge.

Watts, A.B., 2001. Isostasy and Flexure of the Lithosphere. Cambridge University Press, Cambridge.